Richard C. Jaeger
Electrical Engineering Department,
Alabama Micro/Nano Science
and Technology Center,
Auburn University,
Auburn, AL 36849
e-mail: rj@jaegerengineering.com

Mohammad Motalab
Mechanical Engineering Department,
Center for Advanced Vehicle and Extreme
Environment Electronics (CAVE^3),
Auburn University,
Auburn, AL 36849

Safina Hussain
Mechanical Engineering Department,
Center for Advanced Vehicle and Extreme
Environment Electronics (CAVE^3),
Auburn University,
Auburn, AL 36849

Jeffrey C. Suhling
Mechanical Engineering Department,
Center for Advanced Vehicle and Extreme
Environment Electronics (CAVE^3),
Auburn University,
Auburn, AL 36849

Four-Wire Bridge Measurements of Silicon van der Pauw Stress Sensors

Under the proper orientations and excitations, the transverse output of rotationally symmetric four-contact van der Pauw (VDP) stress sensors depends upon only the in-plane shear stress or the difference of the in-plane normal stresses on (100) silicon. In bridge-mode, each sensor requires only one four-wire measurement and produces an output voltage with a sensitivity that is 3.16 times that of the equivalent resistor rosettes or bridges, just as in the normal VDP sensor mode that requires two separate measurements. Both numerical and experimental results are presented to validate the conjectured behavior of the sensor. Similar results apply to sensors on (111) silicon. The output voltage results provide a simple mathematical expression for the offset voltage in Hall effect devices or the response of pseudo Hall-effect sensors. Bridge operation facilitates use of the VDP structure in embedded stress sensors in integrated circuits. [DOI: 10.1115/1.4028333]

Keywords: stress sensor, piezoresistance, van der Pauw, pseudo Hall effect, Wheatstone bridge, (100) silicon, (111) silicon

1 Introduction

Stress effects in four-terminal resistor sensor elements caused by piezoresistance have been of interest to a number of research communities. For example, various piezoresistive structures have been used as sensor elements in pressure sensors [1–6] including the use of the transverse output voltage from four-terminal devices [3–7]. In pressure sensors, the outputs are most often calibrated versus pressure without specific interest in the resolving various stress components in the diaphragm. In contrast, the detailed piezoresistive response of Hall devices, termed the pseudo-Hall effect, has been widely analyzed since it can represent a significant offset error in Hall-effect measurements [8–11].

The electronic packaging community has long been interested in detailed measurement of the various components of the stress state [12–21] in order to understand how to mitigate the impact of stress on precision analog and mixed-signal integrated circuits [22–28] as well as to reduce packaging induced failure of IC die. CMOS compatible sensors are of great interest, and a number of multiterminal resistor and field-effect structures have been proposed for use in extracting the stress state resulting from the packaging of integrated circuits [29–31].

In previous work [32,33], it was demonstrated that standard four-contact VDP structures[1] [34,35] in Fig. 1 could provide partially temperature compensated measurements of in-plane stress components including shear stress σ'_{12} and in-plane normal stress difference $\left(\sigma'_{11} - \sigma'_{22}\right)$ on the (100) silicon surface with greater than 3.16× improvement in sensitivity over corresponding resistor rosettes and bridges. However, stress extraction required two separate measurements of each structure, making the measurements inconvenient and not particularly good for IC implementations.

Other research teams have developed sophisticated ac current spinning techniques and have demonstrated stress extraction from multiterminal sensor structures [9,11,36]. The Hall-effect literature generally presents the stress dependence of the "bridge-mode" outputs but does provide a simple closed-form expression for the magnitude of the sensor output voltage[2] nor discusses the enhanced sensitivity of the symmetrical structure [4,5,7].

There are also important differences between typical Hall devices and the VDP structures that are commonly utilized to measure sheet resistance. The VDP structures are most often designed to be identical under 90 deg rotations in order to simplify the calculations, although the original theory [34,35] only assumes four arbitrarily positioned point-contacts on the periphery. In the Hall effect literature, devices often appear as high aspect ratio rectangular devices with broad contacts on the sides [5,7,37–39], although they can certainly also be square, and there has been much work on the impact of finite width contacts [37–42]. Subsequent analysis presented here based upon superposition requires the use of rotational symmetry.

In this paper, we present numerical and experimental results for four-wire bridge-mode operation of square VDP sensors shown in Fig. 1, and the output voltage is related directly to the results of van der Pauw [34,35]. Current is applied to the devices across one diagonal, and the transverse output voltage is measured across the other diagonal, thereby producing a single four-wire measurement that is directly proportional to either the in-plane shear stress or normal stress difference. The stress dependence of the output depends upon the orientation of the diagonal with respect to the crystallographic axes of silicon [7,11,36]. Bridge-mode operation with dc clearly simplifies the measurements and facilitates use devices as embedded sensors in more complex integrated circuits. Here, we propose that the transverse output voltage is directly

Contributed by the Electronic and Photonic Packaging Division of ASME for publication in the JOURNAL OF ELECTRONIC PACKAGING. Manuscript received March 2, 2014; final manuscript received August 15, 2014; published online September 19, 2014. Assoc. Editor: Satish Chaparala.

[1]We refer to these as van der Pauw sensors since the stress sensor output is directly related to van der Pauw's original voltage and resistivity results.

[2]Often expressed in terms of infinite series.

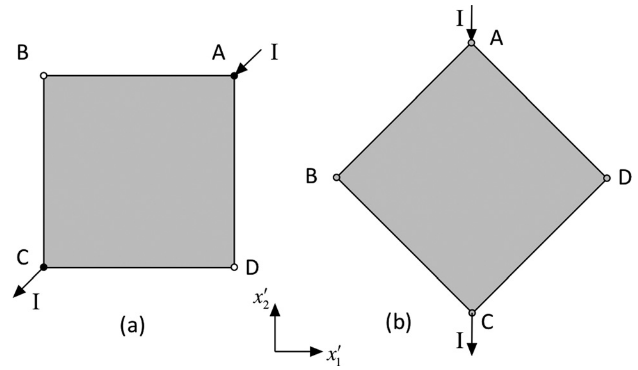

Fig. 1 Square VDP devices at 0 deg and 45 deg orientations. (*a*) $(\sigma'_{11} - \sigma'_{22})$ sensor and (*b*) σ'_{12} sensor. Sensor outputs voltage appear between terminals B and D.

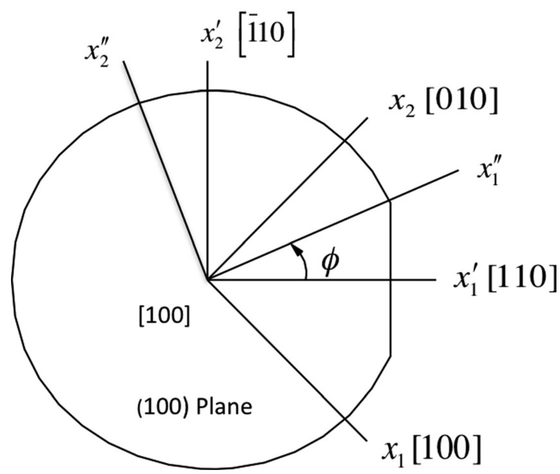

Fig. 2 Principal and primed coordinate systems for (100) silicon

related to the van der Pauw voltage of the isotropic (unstressed) device, and conjecture that the stress dependence of the transverse output voltage is equivalent to the two-step measurement technique in references [32,33] for sensors on both (100) and (111) silicon wafers. The (100) and (111) surface orientations are considered here since they are historically the most common types used in semiconductor manufacturing.

Sections 2 and 3 review modeling of anisotropic electrical conduction in the sensors, and explore electrical symmetries inherent in the structure. In Sec. 4, superposition analysis is used to establish the expected dependencies of the transverse output voltages on stress and the VDP results. Finite element modeling is discussed in Sec. 5, and a commercial finite-element package is used to simulate of the anisotropic conductor. Numerical results in Sec. 6 verify the intuitive results and assumptions made in Sec. 4, and experimental data in Sec. 7 are consistent with our conjectured characterization of the device.

2 Electrical Conduction and Orientation

For two-dimensional electrical conduction problems (i.e., a thin square structure of thickness t) in Cartesian coordinates, voltage Φ must satisfy

$$\kappa'_{11}\frac{\partial^2\Phi}{\partial x_1'^2} + 2\kappa'_{12}\frac{\partial^2\Phi}{\partial x'_1\partial x'_2} + \kappa'_{22}\frac{\partial^2\Phi}{\partial x_2'^2} = I \tag{1}$$

in which the κ'_{ij} represent electrical conductivities in the selected primed coordinate systems in Fig. 2 for (100) and Fig. 3 for (111)

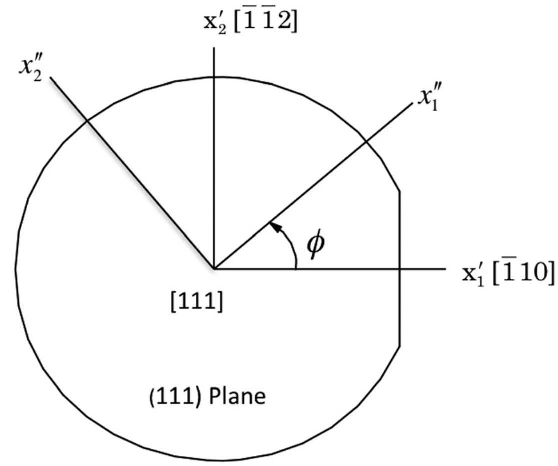

Fig. 3 Primed coordinate system for (111) silicon

silicon wafers, and current I is zero except at the boundary points where current is injected and removed as in Fig. 1. The in-plane axes of the unprimed $(x_1 - x_2)$ coordinate system are aligned with the silicon crystallographic axes, whereas the axes of the primed coordinate system $\left(x'_1 - x'_2\right)$ are aligned with the edges of typical IC chips fabricated on the wafer surface. The x'_3 axis is perpendicular to the silicon wafer. Note that the primed wafer coordinate system in Fig. 2 is rotated from the crystallographic coordinates by 45 deg for (100) silicon material. Similar notation is used for (111) silicon, Fig. 3, but the crystallographic axes are not in the plane of the wafer.

2.1 Resistivity and Conductivity Components. The stress dependence of silicon has traditionally been cast in terms of variation in the resistivity through the three fundamental piezoresistive coefficients: π_{11}, π_{12}, and π_{44}. The in-plane resistivity components have different dependencies on these three coefficients for various semiconductor wafer planes and choice of reference axes. The electrical conductivity components required in Eq. (1) are found from the inverse of the resistivity component matrix

$$\begin{bmatrix} \kappa'_{11} & \kappa'_{12} \\ \kappa'_{12} & \kappa'_{22} \end{bmatrix} = \begin{bmatrix} \rho'_{11} & \rho'_{12} \\ \rho'_{12} & \rho'_{22} \end{bmatrix}^{-1} = \frac{1}{\rho'_{11}\rho'_{22} - \rho_{12}'^2}\begin{bmatrix} \rho'_{22} & -\rho'_{12} \\ -\rho'_{12} & \rho'_{11} \end{bmatrix} \tag{2}$$

2.2 (100) Silicon. The in-plane resistivity components for (100) silicon have been calculated from theory [11,14,30,43], and the general expressions in an arbitrary (double-primed) coordinate system are

$$\begin{aligned} \rho''_{11} &= \rho_o\left[\begin{array}{l} 1 + \frac{\pi_S}{2}\left(\sigma'_{11} + \sigma'_{22}\right) + \frac{\pi_{44}}{2}\left(\sigma'_{11} - \sigma'_{22}\right)\cos 2\phi \\ + \pi_D\sigma'_{12}\sin 2\phi + \pi_{12}\sigma'_{33} + \alpha_1\Delta T \end{array}\right] \\ \rho''_{22} &= \rho_o\left[\begin{array}{l} 1 + \frac{\pi_S}{2}\left(\sigma'_{11} + \sigma'_{22}\right) - \frac{\pi_{44}}{2}\left(\sigma'_{11} - \sigma'_{22}\right)\cos 2\phi \\ - \pi_D\sigma'_{12}\sin 2\phi + \pi_{12}\sigma'_{33} + \alpha_1\Delta T \end{array}\right] \\ \rho''_{12} &= \rho_o\left[\pi_D\sigma'_{12}\cos 2\phi - \frac{\pi_{44}}{2}\left(\sigma'_{11} - \sigma'_{22}\right)\sin 2\phi\right] \\ \pi_D &\equiv \pi_{11} - \pi_{12} \quad \pi_S \equiv \pi_{11} + \pi_{12} \end{aligned} \tag{3}$$

where the stresses are resolved in the primed coordinate system in Fig. 2, ϕ is the angle of rotation of the double-primed coordinate system away from the $x'_1 - x'_2$ axes, and $\Delta T = T - T_{\mathrm{REF}}$ is the temperature change from reference temperature T_{REF}. For this work, the most important terms are the shear resistivities for the two cases in Fig. 1. For the crystallographic system ($\phi = -45$ deg)

Table 1 **Piezoresistive coefficients in lightly doped silicon [44,45]**

Coefficient	n-type Si ($\times 10^{-12}\,\mathrm{Pa}^{-1}$)	p-type Si ($\times 10^{-12}\,\mathrm{Pa}^{-1}$)
π_{11}	−1020	+66
π_{12}	+534	−11
π_{44}	−136	**+1380**
$\pi_S = \pi_{11} + \pi_{12}$	−488	+55
$\pi_D = \pi_{11} - \pi_{12}$	**−1560**	+77
B_1	−311	+718
B_2	+298	−228
B_3	+61	−442
B_1–B_2	**−609**	**+946**
$B_1 = \dfrac{\pi_{11}+\pi_{12}+\pi_{44}}{2}$	$B_2 = \dfrac{\pi_{11}+5\pi_{12}-\pi_{44}}{6}$	$B_3 = \dfrac{\pi_{11}+2\pi_{12}-\pi_{44}}{3}$

Largest values are indicated in bold type.

$$\rho_{12} = \rho_o\left[\frac{\pi_{44}}{2}\left(\sigma'_{11} - \sigma'_{22}\right)\right] \quad (4)$$

whereas the value for $\phi = 0$ deg gives the result in the primed wafer coordinate system

$$\rho'_{12} = \rho_o\left[\pi_D \sigma'_{12}\right] \quad (5)$$

Note that the coordinate systems of interest are associated with the directions of the diagonals of the square sensors.

Values of the piezoresistive coefficients in lightly doped material appear in Table 1 along with two useful combined coefficients, π_D and π_S [43–45]. Note that π_{44} for p-type material and π_D for n-type are the largest of the coefficients, and these differences lead to preferred doping for optimizing the sensitivity of the sensors for a pair of VDP sensors following the suggestions discussed in Refs. [43,46,47] in which the 45 deg sensor would be n-type silicon, and the 0 deg sensor would be p-type.

2.3 (111) Silicon. The in-plane resistivity components for (111) silicon have also been calculated from theory [14,43] and shear resistivities for $\phi = 0$ and 45 deg are

$$\rho'_{12} = \rho_o\left[(B_1 - B_2)\sigma'_{12} + 2\sqrt{2}(B_2 - B_3)\sigma'_{13}\right] \quad (6)$$

and

$$\rho''_{12} = \rho_o\left[\frac{(B_1 - B_2)}{2}\left(\sigma'_{11} - \sigma'_{22}\right) + 2\sqrt{2}(B_2 - B_3)\sigma'_{23}\right] \quad (7)$$

respectively, where the B coefficients are defined in Table 1.

The discussions that follow in the rest of the paper are identical for (100) and (111) silicon except for the numbers and stress terms involved due to the differences in the various coefficients in Eqs. (3)–(7). Note that the (111) sensors contain additional terms related to σ'_{13} and σ'_{23}, although the values of these stress components are zero if the IC die surface is traction free.

3 Electrical Symmetries

A number of electrical symmetries exist when the sensors are carefully aligned to the $x_1 - x_2$ or $x'_1 - x'_2$ coordinate systems defined in Fig. 2, and result in the preferred orientations for the sensors in Fig. 1. These are discussed briefly below. More detailed discussion of the symmetries in terms of standard resistor mesh representations of finite difference equations can be found in Ref. [48].

3.1 Vertical Symmetry. Figure 4 includes a vertical line of symmetry down through the middle of the device relative to the horizontal and vertical resistivity components. Suppose a current I enters the top of the sensor and exits through the bottom. If ρ'_{12} is zero, then the current streamlines will exhibit even symmetry about line AC and be perpendicular to centerline BD. Thus, the voltage V_{BD} across the center of the structure between points B and D will be zero[3] for any values of ρ'_{11} and ρ'_{22}. However, presence of nonzero shear stress ($\rho'_{12} \neq 0$) breaks the symmetry of the structure, and the voltage between B and D depends directly on the shear resistivity in the primed system (Eq. (5))

$$V_{BD} \propto \rho_o \pi_D \sigma'_{12} \quad (8)$$

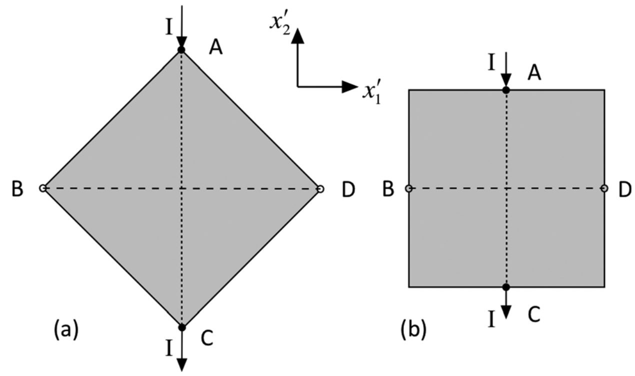

Fig. 4 **Two versions of four-terminal shear stress sensors**

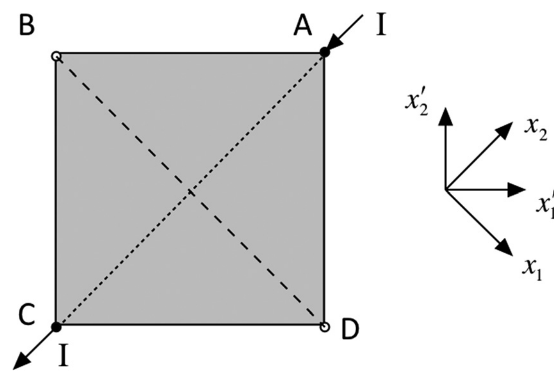

Fig. 5 **The diagonal symmetry line across the square**

The same symmetry applies to the square shape or any rotationally symmetric structure, such as an octagon, and all can potentially be used as shear stress sensors [30,36]. Note that the use of a square structure in Fig. 4(*b*) can be important in state-of-the-art fabrication processes that do not permit creation of ±45 deg geometrical features.

3.2 Diagonal Symmetry. A similar symmetry argument applies to the sensor in Fig. 5 in which current I enters one corner and exits from the diagonally opposite corner. Symmetry now exists relative to the diagonal between corners, and the voltage between points B and D will now depend upon the value of the shear resistivity in the crystallographic coordinate system (Eq. (4)). In this case, output V_{BD} will be proportional to $\pi_{44}\left(\sigma'_{11} - \sigma'_{22}\right)$, and the same symmetry exists for either diagonal

$$V_{BD} \propto \rho_o \pi_{44}\left(\sigma'_{11} - \sigma'_{22}\right) \quad (9)$$

[3] Or between any two symmetrically located points on opposite sides of the device.

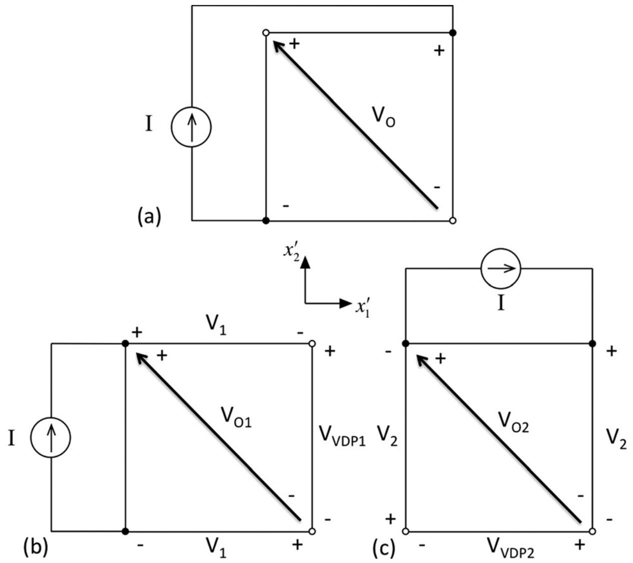

Fig. 6 Analysis by superposition: (*a*) diagonal current excitation and (*b*) + (*c*) equivalent circuits for superposition

Based upon Figs. 4(*b*) and 5, we expect that a single multiterminal square could actually be used to measure temperature compensated values of both shear stress σ'_{12} and the normal stress difference $\left(\sigma'_{11}-\sigma'_{22}\right)$ [11,30,36]. However, one can observe from Table 1 that one of the two sensitivities will be much smaller than that of the other. This is not a limitation in the (111) material where (B_1-B_2) represents the important coefficient for both vertical and diagonal current injection.

Note that the functional dependencies in Eqs. (8) and (9) can also be found by integrating the electric field along paths BC and DC in Figs. 4 and 5. These paths effectively produce bridge outputs involving the resistivities oriented parallel to the edges of the squares.

4 Analysis by Superposition

Electrical behavior of the VDP device is now explored using superposition as depicted in Fig. 6 in which the diagonal current excitation from Fig. 5 is broken into two equal current sources driving the structure along two of the sides of the square. The results of Mian et al. [32,33] apply directly to the two diagrams in Figs. 6(*b*) and 6(*c*).

Using superposition depicted in Fig. 6, we have

$$\begin{aligned} V_{\mathrm{O}} &= V_{\mathrm{O1}}+V_{\mathrm{O2}} \\ V_{\mathrm{O1}} &= V_{\mathrm{VDP1}}+V_1 \text{ and } V_{\mathrm{O2}}=-(V_{\mathrm{VDP2}}+V_2) \end{aligned} \tag{10}$$

Combining these expressions yields

$$V_{\mathrm{O}}=(V_{\mathrm{VDP1}}-V_{\mathrm{VDP2}})+(V_1-V_2) \tag{11}$$

Based upon symmetry for the unstressed isotropic case, $V_{\mathrm{VDP1}}=V_{\mathrm{VDP2}}=V_{\mathrm{VDP}}$ and $V_1=V_2$, where V_{VDP} is the VDP voltage given by VDP's formula for rotationally symmetric structures [34,35]

$$V_{\mathrm{VDP1}}=V_{\mathrm{VDP2}}=V_{\mathrm{VDP}}=IR_{\mathrm{S}}\frac{ln(2)}{\pi} \tag{12}$$

where $R_{\mathrm{S}}=(\rho_o/t)$ is the sheet resistance of the sensor. Therefore, output voltage V_{O} is zero in the isotropic (unstressed) case. A similar analysis applies to the 45 deg sensor.

When stress is present, Refs. [32] and [33] have shown theoretically that the combination of the two separate sets of measurements in Figs. 6(*b*) and 6(*c*) result in Eqs. (13) and (14) for the 0 deg and 45 deg VDP devices on (100) silicon, respectively,

$$V_{\mathrm{VDP1}}-V_{\mathrm{VDP2}}=V_{\mathrm{VDP}}\left[3.16\pi_{44}\left(\sigma'_{11}-\sigma'_{22}\right)\right] \tag{13}$$

$$V_{\mathrm{VDP1}}-V_{\mathrm{VDP2}}=V_{\mathrm{VDP}}\left[3.16(2\pi_D)\sigma'_{12}\right] \tag{14}$$

These output voltage differences provide a 3.16× improvement in sensitivity over the corresponding resistor rosettes and bridges. Thus the transverse output voltages in Eq. (11) across the diagonals of the two structures become

$$\begin{aligned} V_{\mathrm{O/0\,deg}} &= V_{\mathrm{VDP}}\left[3.16\pi_{44}\left(\sigma'_{11}-\sigma'_{22}\right)\right]+\left(V_1^0-V_2^0\right) \\ V_{\mathrm{O/45\,deg}} &= V_{\mathrm{VDP}}\left[3.16(2\pi_D)\sigma'_{12}\right]+\left(V_1^{45}-V_2^{45}\right) \end{aligned} \tag{15}$$

For the unstressed case, the second terms involving V_1 and V_2 in each equation are zero (since $V_1=V_2$ by symmetry as mentioned above). In the next two sections, finite element simulations are used to demonstrate that V_1 and V_2 still cancel out even in stressed sensors, and experimental verification for stressed sensors is given in Sec. 7. However, we have not been able to argue theoretically that V_1 and V_2 are equal in the general stressed condition. Thus, we can only conjecture based upon numerical simulations and sample data that diagonal mode operation yields the desired enhanced sensitivity outputs, but with the advantage that only one four-wire bridge type measurement is required for each stress term. With $V_1-V_2=0$, Eq. (15) becomes

$$\begin{aligned} V_{O/0\,\mathrm{deg}} &= V_{\mathrm{VDP}}\left[3.16\pi_{44}\left(\sigma'_{11}-\sigma'_{22}\right)\right] \\ V_{O/45\,\mathrm{deg}} &= V_{\mathrm{VDP}}\left[3.16(2\pi_D)\sigma'_{12}\right] \end{aligned} \tag{16}$$

Similar analyses for VDP devices on (111) silicon yield

$$\begin{aligned} V_{O/0\,\mathrm{deg}} &= V_{VDP}(3.16)\left[(B_1-B_2)\left(\sigma'_{11}-\sigma'_{22}\right)+4\sqrt{2}(B_2-B_3)\sigma'_{23}\right] \\ V_{O/45\,\mathrm{deg}} &= V_{VDP}(3.16)\left[2(B_1-B_2)\sigma'_{12}+4\sqrt{2}(B_2-B_3)\sigma'_{13}\right] \end{aligned} \tag{17}$$

which also contain terms from two additional out-of-plane shear stress components. These additional terms are zero if the surface of the die is traction free.

4.1 Temperature Compensation. The temperature coefficient of resistance is isotropic, and resistivities ρ''_{11} and ρ''_{22} are affected by temperature in exactly the same way. Hence, a voltage difference taken between any two symmetrically located points on the sensor will be independent of temperature dependent changes (temperature compensated) in the isotropic resistivity. However, it is important to note that this does not apply to the temperature coefficient of the piezoresistive coefficients themselves, which must appear in the output expressions.

5 Finite Element Modeling

The commercial simulation program ABAQUS™ is capable of simulating multidimensional anisotropic heat conduction problems using finite element techniques and is used in this work for simulation of the VDP sensors. For two-dimensional heat conduction problems, temperature T must satisfy

$$k'_{11}\frac{\partial^2 T}{\partial x_1'^2}+2k'_{12}\frac{\partial^2 T}{\partial x'_1\partial x'_2}+k'_{22}\frac{\partial^2 T}{\partial x_2'^2}=Q \tag{18}$$

where the k'_{ij} represent thermal conductivities. Equation (18) is the same as Eq. (1), and the well-known analogies between electrical conduction and heat conduction are listed in Table 2. Thus, in this

Table 2 Analogy between heat conduction and electrical conduction

Heat conduction	Unit	Electrical conduction	Unit
Conductivity k'_{ij}	W/m-K	Conductivity κ'_{ij}	1/Ω-m
Heat flux q'	W/m^2	Current density J'	A/m^2
Temperature T	K	Voltage V	V
Heat flow Q	W	Current I	A

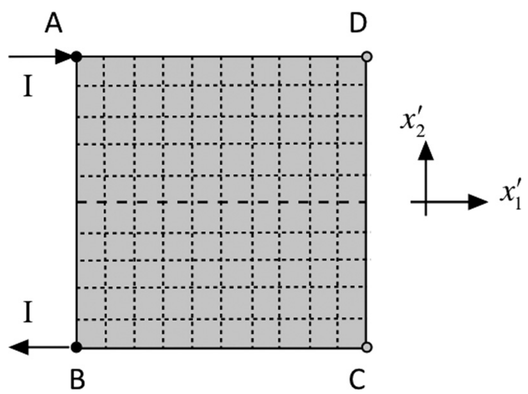

Fig. 7 Initial FEA mesh and current excitation $I = 100\,\mu$A for VDP mode: $R_{VDP} = [\pi/(\ln(2)]\, V_{DC}/I_{AB}$

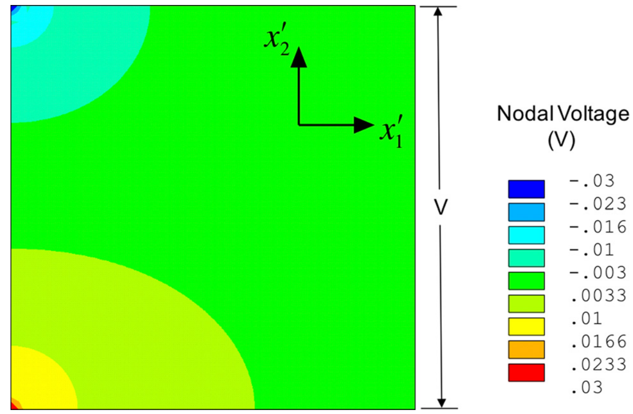

Fig. 8 Contours of potential distribution for VDP sensor

work, the two-dimensional heat conductivity problem has been solved numerically, and the nodal temperature has been extracted as output. This temperature value is equivalent to the voltage in the analogous two-dimensional electrical conduction problem. Simulation results have been used to better understand and verify the intuitive behavior of the square VDP sensors and to confirm the postulated sensitivities of the sensors to various stresses.

5.1 Model Development. Our initial two-dimensional model for the VDP sensor is shown in Fig. 7 and consists of 100 four-node shell conduction elements. The simulation program has steady-state as well as transient heat conduction capabilities and has a single degree of freedom, temperature. The dimensions of the modeled VDP structure are $1000 \times 1000\,\mu$m, and the shell elements have a thickness of $100\,\mu$m. The total heat flow is assumed to be $100\,\mu$W (analogous to an $100\,\mu$A current). The total heat is applied at the corner node points A (heat flow in) and B (heat flow out). Heat flux (analogous to current density) normal to the boundary elsewhere is assumed zero.

The voltage difference between corners D and C is related to the sheet resistance R_S $(= \rho_o/t)$ of the square by VDP's formula in Eq. (12).

5.2 Solution Procedure. The finite element model has been generated in ABAQUS for an orthotropic conductor with conductivity components $\kappa'_{11}, \kappa'_{22}$, and κ'_{12}. For the isotropic case, the resistivity components are $\rho'_{11} = \rho'_{22} = \rho_o$, which is assumed to be 1 $\Omega\cdot$cm and $\rho'_{12} = 0$. Figure 8 shows the potential contours in VDP mode as pictured in Fig. 7. For a sheet resistance of 100 Ω/sq, the theoretical value of the measured VDP resistance should be 22.06 Ω, and simulation yields a value of 22.05 Ω.

To check the dependency of the solution on the finite element mesh, sensitivity tests have been done for this structure. It has been found that if the number of elements is greater than 2500 elements (50×50 array) then the results are independent of the mesh density, so the solutions have converged. All results in this paper were calculated with the 50×50 mesh.

For calculating the stress sensitivites, steady-state conditions have been assumed. It will be demonstrated later that both stress sensor outputs are independent of the variation in ρ'_{11} and ρ'_{22} caused by the temperature dependence of the isotropic resistivity. For different values of the normal stresses $\sigma'_{11}, \sigma'_{22}$, and σ'_{12}, the resistivity components are calculated using Eq. (3) and the resistivity matrices are inverted to get the conductivities for the finite element simulations.

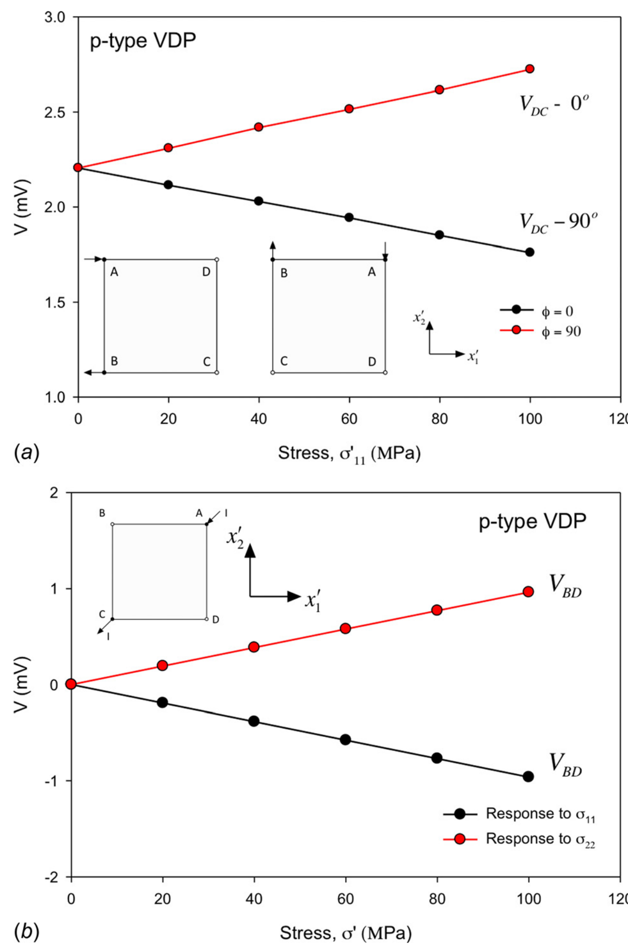

Fig. 9 (*a*) Simulations of the two VDP voltages for 0 deg and 90 deg orientations using the piezoresistive coefficient values in Table 1 for (100) silicon. (*b*) Simulations of the transverse voltages across the diagonal versus stresses σ'_{11} and σ'_{22}.

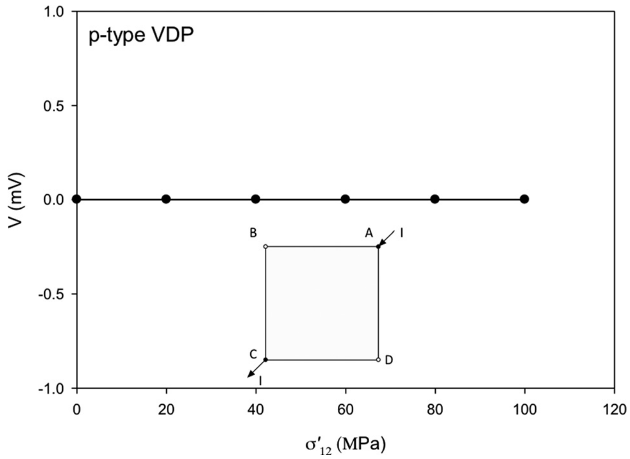

Fig. 10 Simulated output voltage for the $(\sigma'_{11} - \sigma'_{22})$ stress sensor versus shear stress σ'_{12} confirming zero response across the diagonal

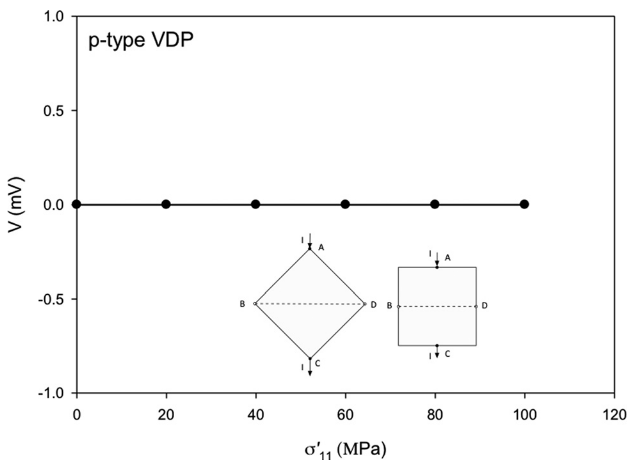

Fig. 11 Simulated output of the shear stress sensors versus normal stress σ'_{11}

6 Simulation Results

This section presents simulation results for a variety of sensor orientations, stress conditions, and temperatures to verify the intuition and analysis presented in Secs. 2–5.

6.1 In-Plane Normal Stress Sensor. Figures 9–14 and Tables 3 and 4 provide simulation results for the two orientations of stress sensors. Figure 9(*a*) shows the VDP output voltages along vertical and horizontal edges versus stress for the 0 deg and 90 deg orientations of the sensor showing that both start at the unstressed value V_{VDP} and spread apart under stress. The individual slopes and intercept agree with the theory presented in Refs. [32] and [33]. The transverse voltage across diagonal BD as plotted in Fig. 9(*b*) agrees closely with the theory in Eq. (15) with $(V_1 - V_2) = 0$ that predicts an output of 0.964 mV for a stress of 100 MPa, based upon the values of π_{44} and π_S in Table 1 with $I = 100\ \mu$A. The slopes of the responses are equal and opposite as expected for σ'_{11} and σ'_{22}.

The simulation results in Tables 3 and 4 give the stress dependent voltages across all four sides of the VDP device when current is injected between adjacent corners. The input voltage and the VDP voltage vary with stress, whereas the other two voltages, identified in as V_1 and V_2 in Sec. 3, are equal and do not vary significantly under stress demonstrating the validity of Eq. (15) with $V_1 - V_2 = 0$. These results have all been rounded to five significant

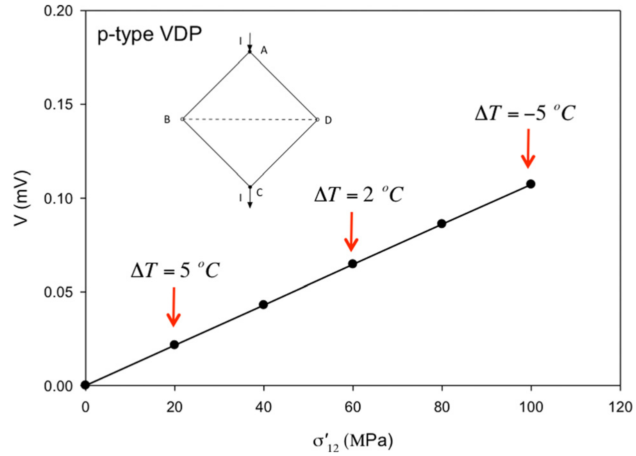

Fig. 12 Simulated output of the shear sensor versus shear stress when temperature variations are present

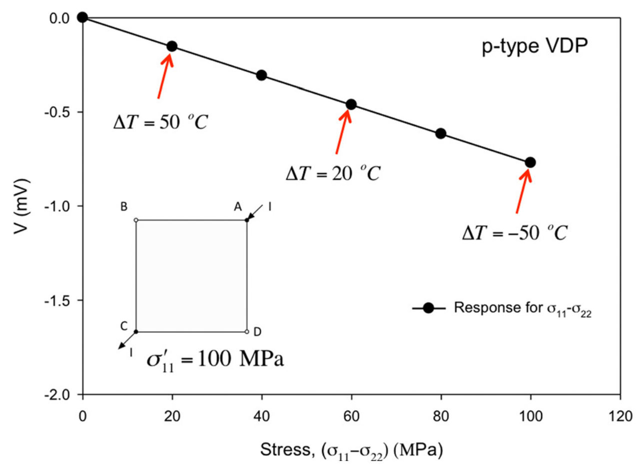

Fig. 13 Transverse output voltage of the normal stress difference sensor versus normal stress $(\sigma'_{11} - \sigma'_{22})$ when temperature variations are present

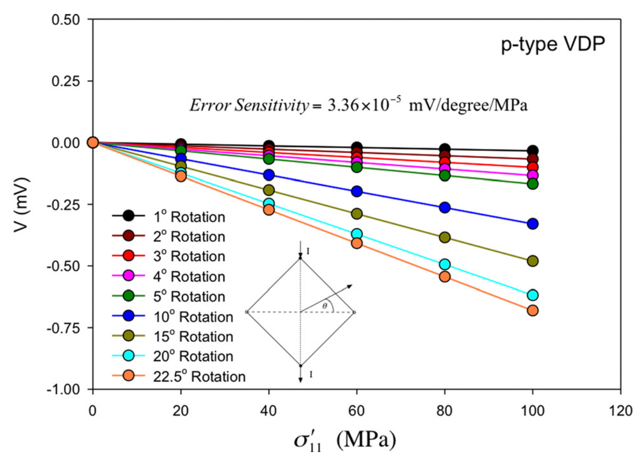

Fig. 14 Simulated output error voltage versus σ'_{11} for rotational misalignment of a shear stress sensor

digits. The maximum deviation from theory is less than 1%. Note that the slopes of the two voltage variations in Fig. 9(*a*) differ slightly since they are proportional to $(\pi_{44} + \pi_S)$and $(\pi_{44} - \pi_S)$ (see Eq. (3)).

Table 3 Simulation results and theory for 0 deg VDP—Fig. 9(a)

Stress (MPa)	V_{AB} (mV)	V_{AD} (V_1) (mV)	V_{CB} (V_1) (mV)	V_{DC} (mV)	Theory (mV)
0	71.737	34.767	34.767	2.205	2.206
20	71.837	34.764	34.764	2.309	2.306
40	71.937	34.762	34.762	2.412	2.407
60	72.038	34.761	34.761	2.516	2.507
80	72.138	34.759	34.759	2.620	2.607
100	72.237	34.757	34.757	2.723	2.707

Table 4 Simulations and theory for 90 deg VDP—Fig. 9(a)

Stress (MPa)	V_{AB} (mV)	V_{AD} (V_2) (mV)	V_{CB} (V_2) (mV)	V_{DC} (mV)	Theory (mV)
0	71.738	34.766	34.766	2.206	2.206
20	71.644	34.764	34.764	2.116	2.114
40	71.552	34.763	34.762	2.026	2.021
60	71.462	34.761	34.761	1.940	1.929
80	71.368	34.759	34.759	1.850	1.837
100	71.275	34.757	34.757	1.761	1.744

Thus, the transverse output voltage of the sensor equals that predicted by Eq. (16) with V_{VDP} defined in Eq. (12). Bridge-mode operation provides the same 3.16 improvement factor over the corresponding resistor sensors as the original VDP stress sensor theory with two sequential measurements of Mian et al. [32,33]. Figure 10 provides numerical verification that the transverse output voltage is in fact independent of shear stress.

6.2 Shear Stress Sensor. Figure 11 presents the output for the shear stress sensors versus normal stress σ'_{11} showing that the output is zero and independent of the in-plane normal stress as predicted. Figure 12 gives the output voltage of the same sensor versus in-plane shear stress σ'_{12} showing a linear output voltage variation with stress. For 100 MPa shear stress with $\pi_D = 77$/TPa, Eq. (16) predicts an output of 0.107 mV, which agrees with the simulation. Note that an n-type sensor would have a much larger output because of the much larger value of π_D. In this case, the simulation results confirm that the transverse output voltage is given by Eq. (16).

The output voltage is proportional to VDP voltage V_{VDP} for the unstressed sensor and the stress induced change. Bridge mode operation again provides the same 3.16 improvement factor over the corresponding resistor sensors as for the original VDP stress sensor theory.

6.3 Temperature Compensation. Figure 12 also depicts the output of the in-plane stress sensor versus stress with large temperature variations included at three points. The points all still remain on a single straight line confirming the temperature compensation of the relations in Eq. (16). Similarly, Fig. 13 depicts the output of the normal stress difference sensor versus stress with

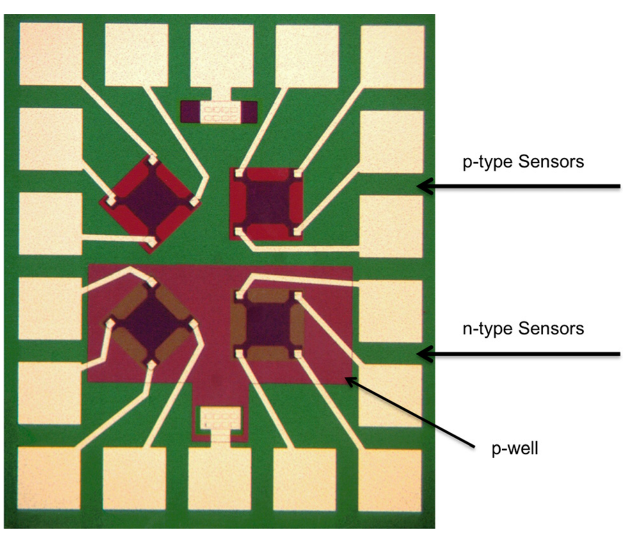

Fig. 15 Microphotograph of a VDP test cell containing 0 deg and 45 deg square n-type and p-type sensors on an n-type substrate. Pads are 100 μm x 100 μm.

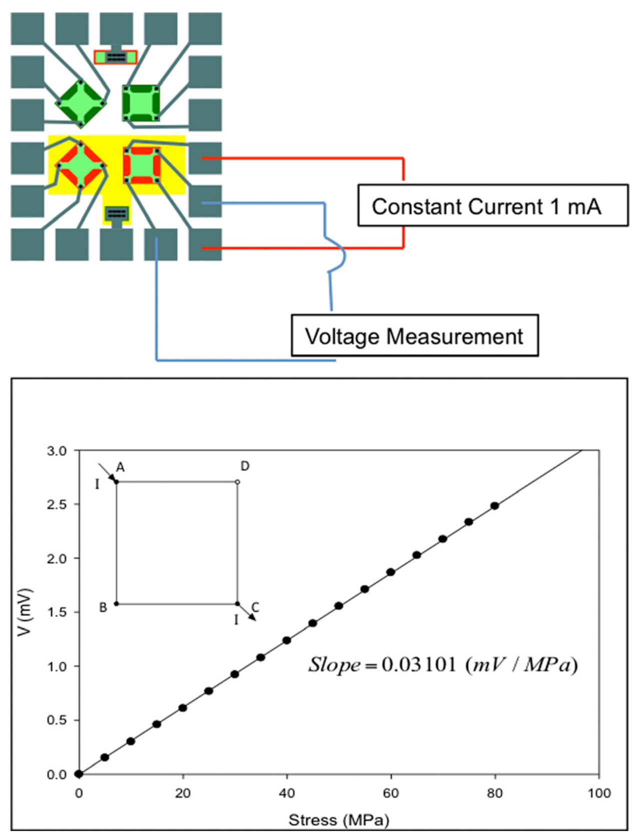

Fig. 16 Measured output of a 0 deg n-type sensor on (111) silicon in bridge mode versus uni-axial stress σ'_{11}

multidegree temperature variations included in the sensor resistivities at three points. Again these intermediate points remain on the linear response supporting the temperature compensation claimed in Eq. (16). It is important to note that temperature dependencies in π_{44} and π_D are not included in the simulations.

6.4 Rotational Alignment Errors. The symmetry results presented earlier for the sensors rely on precise alignment of the sensor edges with respect to the x'_1–x'_2 axes. However, there is a manufacturing tolerance on the wafer flat position relative to the true axes (typically less than 0.5 deg), and there will also be small mask misalignments during the fabrication processes. The error introduced from σ'_{12} coupling into the $\left(\sigma'_{11} - \sigma'_{22}\right)$ output of the normal stress difference sensor can be found from the general resistivity expressions in Eq. (3)

$$V_{\mathrm{ERR}} = 3.16 V_{\mathrm{VDP}} \left(2\pi_D \sigma'_{12}\right) \sin(2\theta) \tag{19}$$

where θ represents the angle of rotation of the square away from the $x'_1 - x'_2$ coordinate system. Similarly, the error introduced from $\left(\sigma'_{11} - \sigma'_{22}\right)$ coupling into the shear stress sensor output can be found as

$$V_{\mathrm{ERR}} = 3.16 V_{\mathrm{VDP}} \pi_{44} \left(\sigma'_{11} - \sigma'_{22}\right) \sin(2\theta) \tag{20}$$

where θ represents the angle of rotation of the diagonals of the shear stress sensor away from the x'_1–x'_2 wafer axes.

Figure 14 presents an example of simulation results for the shear stress sensor output when rotational misalignments ranging from 1 deg to 22.5 deg are added to the orientation of the square shear sensor. A few degrees of error can be tolerated except in regions where stresses are small.

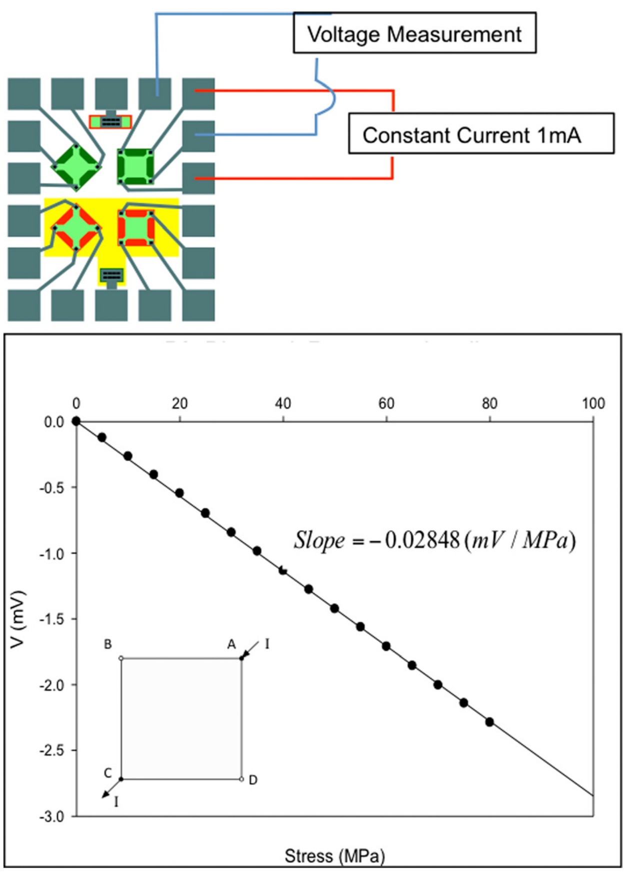

Fig. 17 Measured output of a 0 deg p-type sensor on (111) silicon in bridge mode versus uni-axial stress σ'_{11}

7 Experimental Results

This section presents the results of measurements on various n- and p-type VDP sensors. Figure 15 shows a microphotograph of a VDP test cell containing four VDP test devices that was fabricated on both (100) and (111) silicon. The upper two sensors are p-type silicon and the lower two are n-type. The devices were fabricated on n-type wafers using a basic p-well process, and the sheet resistances were both designed to be approximately 100 Ω/sq.

Equations (16) and (17) contain the relations for the sensor outputs versus stress. The basic behavior of the sensors is the same on (100) and (111) silicon for the condition of uni-axial applied stress, except for the differences between the values of the "π" and "B" coefficients.

Figure 16 presents the output of the 0 deg n-type bridge-mode sensor on (111) silicon as a function of in-plane stress σ'_{11}, and Fig. 17 gives a similar output for a p-type sensor on (111) silicon.

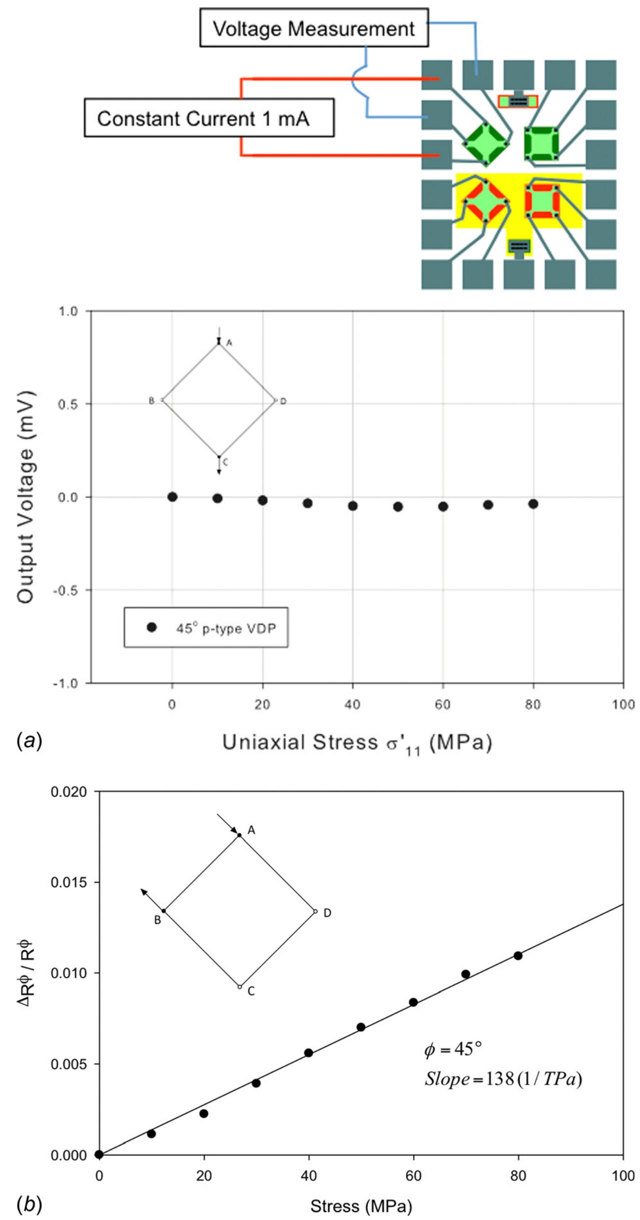

Fig. 18 45 deg p-type stress sensor on (111) silicon. (*a*) Measured transverse output voltage across the sensor showing approximately zero response to σ'_{11}. The worst-case output error is $-54\,\mu$V. (*b*) Measured output of the same shear stress sensor in VDP mode versus uni-axial stress σ'_{11}.

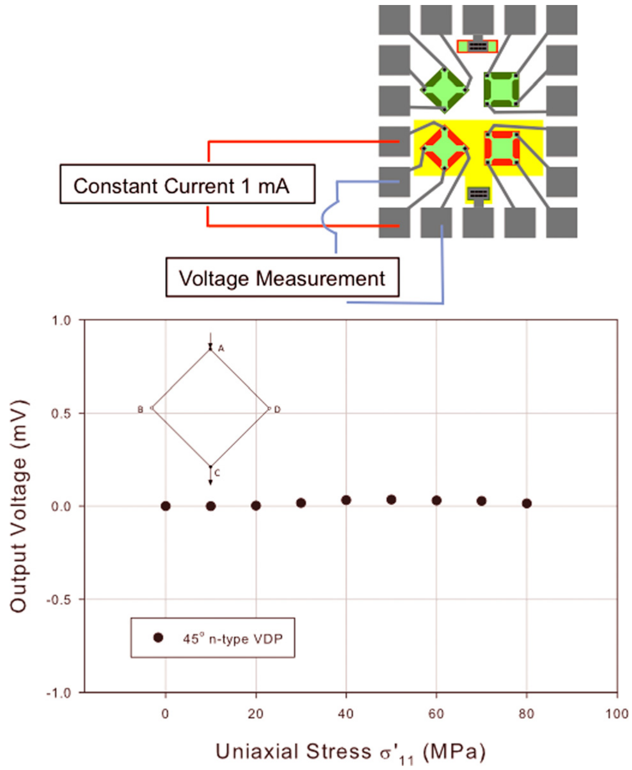

Fig. 19 Measured the transverse voltage output of a 45 deg (111) n-type shear stress sensor versus uni-axial stress showing approximately zero response to σ'_{11}. The maximum output error is 35 μV.

Table 5 0 deg n-type sensor on (111) silicon

Stress (MPa)	V_0	V_{90}	V_0–V_{90}	V_{diag}
0	2.813	2.801	0.012	0.015
10	2.828	2.785	0.043	0.048
20	2.843	2.769	0.074	0.080
30	2.859	2.753	0.106	0.112
40	2.874	2.738	0.136	0.143
50	2.89	2.722	0.168	0.175
60	2.905	2.706	0.199	0.207
70	2.921	2.690	0.231	0.238
80	2.937	2.671	0.266	0.268

$R_S = 127\ \Omega$/sq—all voltages in mV

Note that the slopes of the two sensor outputs are similar in magnitude but opposite in sign. This occurs since the magnitudes of the quantity $(B_1 - B_2)$ are similar for both n- and p-type material on (111) silicon (see Table 1).

Figures 18(*a*) and 19 present the response of the outputs of 45 deg p- and n-type shear stress sensors on (111) silicon to in-plane normal stress showing almost zero change under stress. The graph in Fig. 18(*b*) shows the output for a standard VDP measurement in the presence of uni-axial stress σ'_{11}. The results in Fig. 18(*b*) show that the device is indeed responding to the in-plane normal stress when using the standard VDP sensor approach, but has little or no output in the diagonal mode. The transverse voltages across the diagonals in both Figs. 18(*a*) and 19 are small and are caused by small asymmetries and rotational misalignments.

7.1 Comparison of Transverse Voltage and VDP Voltages.

Tables 5 and 6 present measured results comparing the difference in the two VDP voltages with the voltages across the diagonal for 0 deg n-type and p-type sensors on (111) silicon. Once the small initial offsets are subtracted, the differences in columns four and five are only a few microvolts. The data yield sheet resistances of 80.6 and 127 Ω/sq for the p- and n-type sensors, respectively. From the V_0 and V_{90} data, one obtains values of $(B_1 - B_2)$ of 346/TPa and 616/TPa for the n- and p-type sensors, respectively. These results agree well with data from Mian [49]. The values are on the order of 60% of the maximum values expected for lightly doped silicon and are consistent with the data of Cho et al. [50].

Table 6 0 deg p-type sensor on (111) silicon

Stress (MPa)	V_0	V_{90}	V_0–V_{90}	V_{diag}
0	1.782	1.781	−0.001	−0.001
10	1.770	1.799	0.029	0.028
20	1.758	1.816	0.058	0.057
30	1.745	1.833	0.088	0.086
40	1.734	1.851	0.117	0.115
50	1.722	1.868	0.146	0.144
60	1.710	1.885	0.175	0.173
70	1.697	1.903	0.206	0.202
80	1.689	1.918	0.229	0.230

$R_S = 80.6\ \Omega$/sq—all voltages in mV

8 Summary and Conclusions

Under the proper orientations and excitations, the transverse (diagonal) voltage of symmetrical four-contact VDP sensors depends upon either the in-plane shear stress σ'_{12} or the in-plane normal stress difference $\left(\sigma'_{11} - \sigma'_{22}\right)$ on both (100) and (111) silicon. Other stress terms are canceled out by the symmetry of the structure, and the measurements are inherently temperature compensated.

In bridge-mode, each sensor requires only one four-wire measurement and produces an output voltage with a sensitivity that is 3.16 times that of the equivalent resistor rosettes or bridges, just as in the normal VDP sensor mode that utilizes two separate measurements. The output voltage is proportional to the voltage derived by VDP for an isotropic device. Experimental and finite-element simulation results are consistent with the conjectured mathematical models for the behaviors of the sensors. We hope to find a formal analytical proof in the future.

The simple expressions presented also characterize the output voltage of pseudo Hall effect sensors or equivalently the offset voltage of Hall effect devices caused by piezoresistive effects.

Square sensors offer an advantage for use in small geometry processes that do not permit fabrication of ±45 deg geometrical features, and the two sensors can easily be merged into a single square eight-contact device.

Acknowledgment

This work was supported by the Alabama Micro/Nano Science and Technology Center and the NSF Center for Advanced Vehicle and Extreme Environment Electronics (CAVE³). We want to thank one of the reviewers for the detailed and thoughtful review of the original manuscript that significantly improved the presentation.

References

[1] Mason, W. P., and Thurston, R. N., 1957, "Use of Piezoresistive Materials in the Measurement of Displacement, Force and Torque," J. Acoust. Soc. Am., **29**(10), pp. 1096–1101.

[2] Pfann, W. G., and Thurston, R. N., 1961, "Semiconducting Stress Transducers Utilizing the Transverse and Shear Piezoresistance Effects," J. Appl. Phys., **32**(10), pp. 2008–2019.

[3] Samaun, S., Wise, K., Nielsen, E., and Angell, J., 1971, "An IC Piezoresistive Pressure Sensor for Biomedical Instrumentation," IEEE International Solid-State Circuits Conference, Philadelphia, PA, Feb 17–19, pp. 104–105.

[4] Kanda, Y., and Yasukawa, A., 1982, "Hall-Effect Devices as Strain and Pressure Sensors," Sens. Actuators, **2**, pp. 283–296.
[5] Zhadko, I. P., Babichev, G. G., Kozlovskiy, S. I., Romanov, V. A., Sharan, N. N., and Zinchenko, E. A., 2001, "Silicon Pressure Transducer With Differential Element Based on the Transverse Electromotive Force Effect," Sens. Actuators A, **90**(1–2), pp. 89–95.
[6] Barlian, A. A., Park, W.-T., Mallon, J. R., Rastegar, A. J., and Pruitt, B. L., 2009, "Review: Semiconductor Piezoresistance for Microsystems," Proc. IEEE, **97**(3), pp. 513–552.
[7] Gridchin, A. V., and Gridchin, V. A., 1997, "The Four-Terminal Piezotransducer: Theory and Comparison With the Piezoresistive Bridge," Sens. Actuators A: Phys., **58**(3), pp. 219–223.
[8] Kanda, Y., and Migitaka, M., 1976, "Effect of Mechanical Stress on the Offset Voltages of Hall Devices in Si IC," Phys. Status Solidi A, **35**(2), pp. k115–k118.
[9] Steiner, R., Maier, C., Bellekom, S., and Baltes, H., 1999, "Influence of Mechanical Stress on the Offset Voltages of Hall Devices Operated With Spinning Current Method," J. MEMS, **8**(4), pp. 466–472.
[10] Rise, O., Shaked, E., Karpovsky, M., and Gerber, A., 2008, "Offset Reduction in Hall Effect Measurements Using a Nonswitching van der Pauw Technique," Rev. Sci. Instrum., **79**(7), p. 073901.
[11] Bartholomeyczik, J., Doelle, M., Ruther, P., and Paul, O., 2009, "Cartesian Lattice Spinning Current Method for the Simple Extraction of σ_{xx}-σ_{yy} and σ_{xy} Stresses and the Hall Voltage From Four-Contact Elements," 13th International Conference on Solid-State Sensors, Actuators and Microsystems (TRANSDUCERS'05), New York, June 5–9, pp. 2127–2130.
[12] Spencer, J. L., Schroen, W. H., Bednarz, G. A., Bryan, J. A., Metzgar, T. D., Cleveland, R. D., and Edwards, D. R., 1981, "New Quantitative Measurements of IC Stress Introduced by Plastic Packages," 19th IEEE Annual Reliability Physics Symposium, Las Vegas, NV, Apr. 7–9, pp. 74–80.
[13] Gee, S. A., van den Bogert, W. F., and Akylas, V. R., 1989, "Strain-Gauge Mapping of Die Surface Stresses," IEEE Trans. Comp., Hybrids, Manuf. Technol., **12**(4), pp. 587–593.
[14] Bittle, D. A., Suhling, J. C., Beaty, R. E., Jaeger, R. C., and Johnson, R. W., 1991, "Piezoresistive Stress Sensors for Structural Analysis of Electronic Packages," ASME J. Electron. Packag., **113**(3), pp. 203–215.
[15] Sweet, J. N., 1993, "Die Stress Measurement Using Piezoresistive Stress Sensors," *Thermal Stress* and *Strain in Microelectronics Packaging*, J. H. Lau, ed., von Nostrand Reinhold, New York, pp. 221–271.
[16] Gestel, R. V., 1994, *Reliability Related Research on Plastic IC Packages: A Test Chip Approach*, Delft Technical University, Delft, Netherlands.
[17] Zou, Y., Suhling, J. C., Jaeger, R. C., and H. Ali, 1998, "Three Dimensional Die Surface State Measurements in Delaminated and Non-Delaminated Plastic Packages," 48th IEEE Electronic Components and Technology Conference, Seattle, WA, May 25–28, pp. 1223–1234.
[18] Zou, Y., Suhling, J. C., Johnson, R. W., Jaeger, R. C., and Mian, A. K. M., 1999, "In-Situ Stress State Characterization During Chip-on-Board Assembly," IEEE Trans. Electron. Packag. Manuf., **22**(1), pp. 38–52.
[19] Doelle, M., Peters, C., Ruther, P., and Paul, O., 2006, "Piezo-FET Stress Sensor Arrrays for Wire Bonding Characterization," IEEE J. MEMS, **15**(1), pp. 120–130.
[20] Baumann, M., Gieschke, P., Lemke, B., and Paul, O., 2010, "CMOs Sensor Chip With a 10×10 Array of Unit Cells for Mapping Five Stress Components and Temperature," IEEE 23rd International Conference Micro Electro Mechancial Systems, (MEMS), Wanchai, Hong Kong, Jan. 24–28, pp. 604–607.
[21] Chen, Y., Jaeger, R. C., and Suhling, J. C., 2013, "CMOS Sensor Arrays for High Resolution Die Stress Mapping in Packaged Integrated Circuits," IEEE Sens. J., **13**(6), pp. 2066–2076.
[22] Hamada, T. F., Saito, N., and Takeda, E., 1991, "A New Aspect of Mechanical Stress Effects in Scaled MOS Devices," IEEE Trans. Electron Devices, **38**(4), pp. 895–900.
[23] Jaeger, R. C., Ramani, R., and Suhling, J. C., 1995, "Effects of Stress-Induced Mismatches on CMOS Analog Circuits," International Symposium on VLSI Technology, Systems, and Applications, Taipei, Taiwan, May 31–June 2, pp. 354–360.
[24] Ali, H., 1997, "Stress-Induced Parametric Shift in Plastic Packaged Devices," IEEE Trans. Comp., Packag. Manuf. Technol., Part B, **20**(4), pp. 458–462.
[25] Bastos, J., Steyaert, M. S. J., Pergoot, A., and Sansen, W. M., 1997, "Influence of Die Attachment on MOS Transistor Matching," IEEE Trans. Semicond. Manuf., **10**(2), pp. 209–218.
[26] Jaeger, R. C., Bradley, A. T., Suhling, J. C., and Zou, Y., 1997, "FET Mobility Degradation and Device Mismatch Due to Packaging Induced Die Stress," 23rd European Solid-State Circuits Conference (ESSCIRC'97), Southampton, UK, Sept. 16–18, pp. 272–275.
[27] Tuinhout, H. P., and Vertregt, M., 2001, "Characterization of Systematic MOSFET Current Factor Mismatch Caused by Metal CMP Dummy Structures," IEEE Trans. Semicond. Manuf., **14**(4), pp. 302–310.
[28] Fruett, F., Meijer, G. C. M., and Bakker, A., 2003, "Minimization of the Mechanical-Stress-Induced Inaccuracy in Bandgap Voltage References," IEEE J. Solid-State Circuits, **38**(7), pp. 1288–1291.
[29] Jaeger, R. C., Suhling, J. C., Ramani, R., Bradley, A. T., and Xu, J., 2000, "CMOS Stress Sensors on (100) Silicon," IEEE J. Solid-State Circuits, **35**(1), pp. 85–95.
[30] Bartholomeyczik, J., Brugger, S., Ruther, P., and Paul, O., 2005, "Multidimensional CMOS In-Plane Stress Sensor," IEEE Sens. J., **5**(5), pp. 872–882.
[31] Baumann, M., Lemke, B., Ruther, P., and Paul, O., 2009, "Piezoresistive CMOS Sensor for Out-of-Plane Shear Stress," 2009 IEEE Sensors Conference, Christchurch, New Zealand, Oct. 25–28, pp. 441–444.
[32] Mian, A., Suhling, J. C., Jaeger, R. C., and Wilamowski, B. M., 1997, "Evaluation of Die Stress Using van der Pauw Sensors," ASME International Mechanical Engineering Congress and Exposition, Dallas, TX, Nov. 16–21, EEP-Vol. 22, pp. 59–67.
[33] Mian, A. K. M., Suhling, J. C., and Jaeger, R. C., 2006, "The van der Pauw Stress Sensor," IEEE Sens. J., **6**(2), pp. 340–356.
[34] van der Pauw, L. J., 1958, "A Method of Measuring Specific Resistivity and Hall Effect of Disks of Arbitrary Shape," Philips Res. Rep., **13**(1), pp. 1–9, available at: http://aki.issp.u-tokyo.ac.jp/okano/WalWiki/etc/VDP_PRR_13_1.pdf
[35] van der Pauw, L. J., 1961, "Determination of Resistivity Tensor and Hall Tensor of Anisotropic Conductors," Philips Res. Rep., **16**, pp. 187–195.
[36] Bartholomeyczik, J., Kibbel, S., Ruther, P., and Paul, O., 2005, "Extraction of Compensated σ_{xx}-σ_{yy} and σ_{xy} Stresses From a Single Four-Contact Sensor Using the Spinning Transverse Voltage Method," 18th IEEE International Conference on Micro Electro Mechanical Systems, 2005 (MEMS 2005), Miami, FL, Jan. 30–Feb. 3, pp. 263–266.
[37] Doelle, M., Mager, D., Ruther, P., and Paul, O., 2006, "Geometry Optimization for Planar Piezoresistive Stress Sensors Based on the Pseudo-Hall Effect," Sens. Actuators A, **127**(2), pp. 261–269.
[38] Versnel, W., 1979, "Analysis of the Greek Cross, a van der Pauw Structure With Finite Contacts," Solid-State Electron., **22**(11), pp. 911–914.
[39] Versnel, W., 1981, "Analysis of Symmetrical Hall Plates With Finite Contacts," J. Appl. Phys., **52**(7), pp. 4659–4666.
[40] Versnel, W., 1982, "The Geometrical Correction Factor for a Rectangular Hall Plate," J. Appl. Phys., **53**(7), pp. 4980–4986.
[41] Chwang, R., Smith, B. J., and Crowell, C. R., 1974, "Contact Size Effects on the van der Pauw Method for Resistivity and Hall Coefficient Measurement," Solid-State Electron., **17**(12), pp. 1217–1227.
[42] Koon, D. W., 1989, "Effect of Contact Size and Placement, and of Resistive Inhomogenities on van der Pauw Measurements," Rev. Sci. Instrum., **60**(2), pp. 271–274.
[43] Suhling, J. C., and Jaeger, R. C., 2001, "Silicon Piezoresistive Stress Sensors and Their Application in Electronic Packaging," IEEE Sens. J., **1**(1), pp. 14–30.
[44] Smith, C. S., 1953, "Piezoresistance Effects in Germanium and Silicon," Phys. Rev., **94**(1), pp. 42–49.
[45] Tufte, O. N., and Stelzer, E. L., 1963, "Piezoresistive Properties of Silicon Diffused Layers," J. Appl. Phys., **34**(2), pp. 3322–3327.
[46] Cordes, R. A., Suhling, J. C., Kang, Y., and Jaeger, R. C., 1995, "Optimal Temperature Compensated Piezoresistive Stress Sensor Rosettes," Symposium on Applications of Experimental Mechanics to Electronic Packaging, ASME IMECE, AMD-Vol-214, pp. 109–116.
[47] Jaeger, R. C., Suhling, J. C., and Ramani, R., 1994, "Errors Associated With the Design, Calibration and Application of Piezoresistive Stress Sensors in (100) Silicon," IEEE Trans. CPMT B, **17**(1), pp. 97–107.
[48] Jaeger, R. C., Motalab, M., Hussain, S., and Suhling, J. C., 2013, "Four-Wire Bridge Measurements of van der Pauw Stress Sensors on (100) and (111) Silicon," ASME Paper No. IPACK2013-73249.
[49] Mian, A. K. M., 2000, Application of the van der Pauw Structure as a Piezoresistive Stress Sensor, Ph.D. dissertation, Auburn University, Auburn, AL.
[50] Cho, C.-H., Jaeger, R. C., and Suhling, J. C., 2008, "Characterization of the Temperature Dependence of the Piezoresistive Coefficients of Silicon From $-150\,^{\circ}$C to $+125\,^{\circ}$C," IEEE Sens. J., **8**(8), pp. 1455–1468.